The Astrophysical Journal Supplement Series, 267:12 (13pp), 2023 July https://doi.org/10.3847/1538-4365/acd117

Critically Evaluated Atomic Data for the Au IV Spectrum

Aashna Zainab[1], K. Haris[1], Sébastien Gamrath[2], Pascal Quinet[2,3], and A. Tauheed[1]
[1] Department of Physics, Aligarh Muslim University, Aligarh, UP 202002, India; kharisphy@gmail.com, kharis.ph@amu.ac.in
[2] Physique Atomique et Astrophysique, Université de Mons, B-7000 Mons, Belgium
[3] IPNAS, Université de Liège, B-4000 Liège, Belgium
Received 2022 July 29; revised 2023 April 1; accepted 2023 April 24; published 2023 July 5

Abstract

A spectral investigation of triply ionized gold (Au IV) has been carried out in the wavelength region of 500–2106 Å. The gold spectra were photographed at the National Institute of Standards and Technology, USA, on a 10.7 m normal incidence vacuum spectrograph (NIVS) using a sliding spark source as well as on a 3 m NIVS at the Antigonish laboratory in Canada with a triggered spark source. Our analysis is theoretically supported by the pseudorelativistic Hartree–Fock (HFR) formalism with a superposition of configuration interactions implemented in Cowan's suite of codes. Radiative transition parameters are also calculated using the HFR+CPOL (core polarization effects) model and the multiconfiguration Dirac–Hartree–Fock approach, and their comparisons are used to evaluate the transition rate data. All the previously reported levels of the $5d^8$, $5d^7 6s$, and $5d^7 6p$ configurations are confirmed, except one, and three are newly established. The missing $^1S_0$ level of $5d^8$ is now established at 55,277.8 cm^{-1}. A total of 981 observed lines (E1 type), classified to 1031 transitions, including 133 newly identified, enabled us to optimize 139 energy levels. Several astrophysically important transitions, forbidden (M1- and E2-type) lines of $5d^8$ and $5d^7 6s$, are provided with their Ritz wavelengths and radiative parameters. A critically evaluated set of energy levels, observed and Ritz wavelengths along with their uncertainties, transition rates, and uniformly scaled intensities of Au IV lines have been presented. Also, large-scale atomic data to compute the opacity of Au IV in the kilonova ejecta have been supplemented in this work.

Unified Astronomy Thesaurus concepts: Atomic physics (2063); Atomic spectroscopy (2099); Line intensities (2084); Line positions (2085); Transition probabilities (2074); Spectral line identification (2073); Atomic data (2216); Atomic data benchmarking (2064)

Supporting material: machine-readable tables

1. Introduction

The high-resolution spectra of chemically peculiar stars obtained with the Goddard High Resolution Spectrograph on board the Hubble Space Telescope has rekindled the interest in the spectroscopy of high-Z elements. The rich spectrum of the Hg–Mn χ Lupi stars is made up of the spectra of singly and doubly ionized elements with empty $4d$ and $5d$ subshells whose atomic structures are quite complex (Leckrone et al. 1993). To obtain an accurate data set for these elements, it has been proposed that their spectral research must be supported by the energy parameter regularities in their isoelectronic sequence (Wyart et al. 1993a). Consequently, Wahlgren et al. (1995) summarized the elemental abundances of Pt, Au, and Hg in these chemically peculiar stars, and Au abundances were estimated from the observation of a few selected lines of Au II and Au III. Au I and Au II have simple structures, but the spectrum of Au III and the spectra of its higher-charge stages are very dense, and they overlap each other. In such cases, spectroscopic analysis of adjacent charge states is highly useful and aids the accurate line identification for the spectrum under investigation. Besides, the laboratory studies of heavier elements ($Z \geqslant 54$) including gold have also gained high astrophysical interest after the detection of the gravitational waves by the LIGO/Virgo collaboration, as its observations "GW170817" and the following kilonova "AT2017gfo" support the hypothesis that neutron-star mergers (NSMs) can account for the nucleosynthesis of these heavy elements by the r-process (Abbott et al. 2017; Kasen et al. 2017; Kajino et al. 2019). To explain and model the observed AT2017gfo spectra, large sets of calibrated atomic data are needed for elements beyond iron peak ($Z > 30$), including data on their ionization species (II–V). In this regard, large-scale atomic data for computing the bound–bound opacities of r-process ejecta elements have been given by Kasen et al. (2017), Tanaka et al. (2018, 2020), and Fontes et al. (2020), but data for neutral gold (Au) and its ions (Au II–IV) were only included in the work of Tanaka et al. (2020). Recently, Bromley et al. (2020) and McCann et al. (2022) have provided more calibrated atomic data for Au I–III ions, and Gillanders et al. (2021) have used these data together with data on Pt I–III to estimate the Au/Pt abundances in the ejecta of AT2017gfo for photospheric and nebular phases. For photospheric modeling, data on allowed electric dipole transitions could be important, while Gillanders et al. (2021) have manifested that accurate data on the radiative parameters of forbidden lines are important to interpret the observed kilonova AT2017gfo spectra of late epochs, $t \geqslant +3$ days, and/or of NSM ejecta with low temperatures and densities. Besides these, transition rates of electric and magnetic dipole transitions in Au IV were reported by Taghadomi et al. (2022) using GRASP code calculations. These authors also showed the expansion opacity of Au IV for kilonova ejecta at time $t = 1$ day and for temperature $T = 3700$ K and density $\rho = 10^{-13}$ g cm^{-3}.

In terms of astrophysical observations, the presence of gold (Au I–II) has been confirmed in the environments of various

astrophysical objects, but so far only its allowed transitions have been detected and no forbidden lines have been observed yet in the spectra of astrophysical objects (see the details in Wahlgren et al. 1995; Gillanders et al. 2021). It should be noted that at present radiative parameters of forbidden transitions are reported only for Au I–III spectra, and no such data are available for Au IV. Also, our survey on the forbidden spectrum of Au IV shows that its several lines fall in the visible–IR (0.5–28 μm) operating region of the recently launched James Webb Space Telescope (JWST), and the role of JWST will be instrumental for future kilonova observations in the IR region (Bartos et al. 2016), similar to the observations made by the Spitzer Space Telescope for the "GW170817" NSM event (Villar et al. 2018; Wu et al. 2019; Kasliwal et al. 2022). Therefore, from the laboratory to astrophysics, accurate data on energy levels, wavelengths, intensities, and transition rates are greatly needed for various applications (Wahlgren 2011), including estimating the abundances of *r*-process elements in the kilonova ejecta (Vieira et al. 2023). These data are also used for improving the accuracy of theoretical calculations of complex atoms/ions. Thus, the present work aims to provide critically evaluated spectral data for triply ionized gold (Au IV) belonging to the 5*d*-series elements.

Au IV is a member of the Os I isoelectronic sequence. Its ground configuration is [Xe] $4f^{14}5p^{6}5d^{8}$, which consists of nine energy levels: $^{3}F_{4,3,2}$, $^{3}P_{2,1,0}$, $^{1}D_{2}$, $^{1}G_{4}$, and $^{1}S_{0}$, among which $^{3}F_{4}$ is the lowest. The regular excited configurations, formed by the excitation of one electron from the 5*d* subshell, are of the type $5p^{6}5d^{7}nl$ ($n \geqslant 5$, $l \geqslant 0$). Promotion of two or three electrons leads to complex configurations such as $5d^{6}6s^{2}$, $5d^{6}6p^{2}$, $5d^{6}6s6p$, and $5d^{5}6s^{2}6p$. These configurations are incorporated in the theoretical calculations for better accuracy.

The first spectral analysis that provided an insight into the energy level structure of Au IV was performed by Joshi et al. (1991). They studied the $5d^{8}$–$5d^{7}6p$ transition array in the wavelength region of 554–850 Å. Wyart et al. (1994) provided an extended analysis of the Au IV spectrum by identifying about 700 lines of the $(5d^{8} + 5d^{7}6s)$–$5d^{7}6p$ transition array in the wavelength region of 554–2080 Å. They established 33 (out of 38) energy levels of the $5d^{7}6s$ configuration and increased the known levels of $5d^{7}6p$ from 64 to 95. Apart from these, the 4*f* and 5*p* photoabsorption spectra of Au IV have been studied in the wavelength region of 98–180 Å using a dual laser plasma technique (Su et al. 2009). This work is beyond the scope of our investigation, therefore we did not include it in this critical evaluation.

In this work, we have critically evaluated all the previously reported data on Au IV using the spectrum recorded on a 10.7 m normal incidence vacuum spectrograph (NIVS), and also by providing a theoretical support for our observations within the pseudorelativistic Hartree–Fock (HFR) approach, and the effects of core polarization (CPOL) are accounted for in computing the accurate transition rates for the Au IV spectrum. We aim to provide the wavelengths of observed lines (together with their Ritz counterparts), the optimized energy levels with their uncertainties, uniformly scaled intensities, and transition rates for observed and possibly observable lines of both allowed and forbidden types. The latter types are intra- and inter-configuration transitions between the levels of $5d^{8}$ and $5d^{7}6s$, but may have implications in astrophysics, in particular interpreting the visible and near-IR parts of the kilonova spectra associated with NSM events (Gillanders et al. 2021).

2. Experimental Details

The spectral plates used for this work were the same as those used for the previous analysis of Au III by Zainab & Tauheed (2019). Nevertheless, the necessary details regarding the spectrograms and their recording are provided here for completeness. The recording of the gold spectra, in the region of 500–2106 Å, was performed on a 10.7 m NIVS at the National Institute of Standard and Technology (NIST), USA, using a sliding spark as the excitation source. The spectrograph was equipped with a 1200 lines per millimeter grating that had a first-order reciprocal dispersion of 0.78 Å mm^{-1}. The gold spectra were also recorded at the Antigonish laboratory on a 3 m NIVS with reciprocal dispersion of 1.385 Å mm^{-1} using a triggered spark source. The latter was used just for the purpose of ionization separation. Kodak short-wave radiation (SWR) plates were used for the recording of the spectra. Several tracks of exposures were taken on each plate by varying the experimental conditions, which were achieved by either adjusting the capacitor's charging potential or by inserting inductor coils in series with the discharge circuit. The variation in line intensity at different discharge settings allowed for a satisfactory ionization separation. The track with the strongest Au IV lines was used to measure the wavelengths and the remaining tracks on each plate were used to accomplish the ionization separation. The relative positions of the spectral lines along with their relative visual intensities were measured on a Zeiss Abbe comparator at Aligarh Muslim University, Aligarh. The calibration of the spectrograms was then carried out using reference lines of C II–IV, Si II–IV, Al II–III, and O II–V (Kramida et al. 2022a), together with some Au II lines (Rosberg & Wyart 1997). The general estimate of wavelength uncertainty is due to the combined effect of the statistical deviation of the line position measured on the comparator and the systematic uncertainty of the reference wavelengths used in the fitting. The final wavelength uncertainty for sharp and unperturbed lines is estimated to be better than 0.005 Å and the figure has been doubled for all perturbed lines.

The spectral lines' intensities were visual estimates representing the photographic emulsion blackening. To bring these intensities to a uniform scale, intensity modeling was performed (see Section 5).

3. Analysis of the Spectrum

The first spectroscopic analysis of Au IV was carried out by Joshi et al. (1991) using the spectra recorded on a 6.65 m NIVS at the Zeeman Laboratory and on a 3 m NIVS at the Antigonish laboratory in the wavelength region of 554–850 Å. For both the cases, a triggered spark was used as the excitation source. Several exposures were recorded on Kodak SWR plates with different experimental conditions. The relative positions of the spectral lines were measured on Cospinsca or Grant semiautomatic comparators and the line intensity is reported on a scale of 1 to 99. The wavelength calibration was done using the internal standards of carbon, oxygen, and silicon ion lines, and their measured wavelength uncertainty was 0.005 Å. On the basis of the classification of 196 lines, eight out of nine levels of $5d^{8}$ and 64 out of 110 levels of $5d^{7}6p$ configuration were reported by them.

In the extended analysis of the Au IV spectrum, Wyart et al. (1994) reported the lines belonging to the $5d^{7}6s$–$5d^{7}6p$

transition array in the region of 1020–1930 Å. The spectrograms were recorded on a 10.7 m NIVS of the National Bureau of Standards (now known as NIST), USA, having 0.78 Å mm^{-1} as the reciprocal dispersion. A sliding spark was used as the excitation source, which was operated in different experimental conditions to achieve ionization separation. The spectrograms were measured on a semiautomatic comparator at Observatoire de Paris-Meudon and were calibrated using the reference standards of Cu (a copper hollow cathode spectrum was recorded on the same plates), Si, C, N, and Al. The accuracy of this measurement was quoted as ±0.007 Å. Additional gold plates, recorded by Joshi et al. (1991) on the same experimental setup in the wavelength region of 554–2080 Å, were also supplemented to support the analyses. In the $5d^7 6s$–$5d^7 6p$ transition array, a total of 657 lines, and between $5d^8$–$5d^7 6p$ configurations, 47 newly classified lines were reported by them. This led to the establishment of 33 out of 38 energy levels of $5d^7 6s$ configuration and, among the $5d^7 6p$ levels, two were revised and 31 were newly established.

Our investigation started with the verification of the previously reported data on Au IV. In total, 139 energy levels belonging to the $5d^8$, $5d^7 6s$, and $5d^7 6p$ configurations have been confirmed. A total of 981 observed lines classified to 1031 transitions were used to obtain the optimized energy levels of the Au IV spectrum. All classified lines of Au IV are assembled in Table 1 with their observed wavelengths and uncertainties. The optimized energy levels of Au IV are given in Table 2. The major findings of our present analysis are summarized below:

One level of $5d^7 6p$ configuration with $J = 2$, reported earlier by Joshi et al. (1991) at ≈188,525 cm^{-1}, is now revised to 188,170.6 cm^{-1} with the aid of five transitions. We are also successful in establishing the missing $^1S_0$ level of the $5d^8$ configuration. This level was already known in the Hg V (Wyart et al. 1993b), Tl VI (Raassen et al. 1994a), Pb VII (Raassen et al. 1994b), and Bi VIII (Kildiyarova et al. 1995) ions, thus it was possible to recalculate all the Slater parameters of this configuration and enhance the accuracy of its predicted value along the isoelectronic sequence. Therefore, after eliminating the previously classified lines in the expected region, the level was established at 55,277.8 cm^{-1} and is supported by six Au IV transitions. This energy level value compares well with 55,391 cm^{-1}, which was predicted by Wyart et al. (1993a) based on the orthogonal operator treatment. The determination of the $5d^8$ $^1S_0$ level resulted in new calculation parameters for the ground configuration (see Section 6.1). Additionally, two new levels of $5d^7 6p$ configuration with $J = 0$ were established at 140,590.70 cm^{-1} and 149,963.62 cm^{-1} on the basis of four and three transitions, respectively. These observed lines were weak in our spectrograms, but they exhibited a distinct Au IV character similar to that of other previously classified Au IV lines that appeared in these spectrograms.

4. Optimization of Energy Levels

The least-squares level optimization procedure was done by using the computer code LOPT (Kramida 2011), which helps in obtaining the best fitted energy level values for all observed lines. This process also checks the consistency of the line classifications, by comparing the observed wavelengths with their corresponding Ritz values. A thorough description of this method can be found in several previous publications (Kramida 2013a, 2013b, 2013c; Haris et al. 2014). The optimization procedure was started by including only the previously classified lines of Au IV that led to an initial estimate of the energy level values and Ritz wavelengths of several possibly observable lines with their uncertainties. These lines were searched out in our line list and the obtained lines (about 130) along with their satisfactory character and intensities were added to the optimization procedure. The entire process involves several iterations of level optimization; consequently, the best optimized energy values and uncertainties were obtained for 139 levels (see Table 2), with the help of 981 distinct lines that are classified to 1031 transitions (see Table 1). To determine the final level uncertainties given in Table 2, the $5d^7(^4P)6s$ $^5P_3$ level at 68,890.98 cm^{-1} was selected as a base level, because this level has the maximum number of accurately measured transitions.

Using these results, the final Ritz wavelengths (λ_{Ritz}) with their estimated uncertainties were computed for all observed and several possibly observable lines (see Table 1). These counterpart (i.e., λ_{Ritz}) wavelengths are at least twice as accurate (or more) than the observed ones, therefore they served as reference lines to check the internal consistencies of previous measurements (Joshi et al. 1991; Wyart et al. 1994). The results of these comparisons are shown in Figures 1 and 2. The suitable systematic correction curves were made with the help of different polynomial fits (see the captions of Figures 1 and 2), and the corrected wavelengths of previous measurements are provided in Table 1. The agreement between the corrected and Ritz wavelengths was found to be satisfactory within a standard deviation of 0.005 Å, which fairly agrees with their original claimed accuracy.

5. Reduction of Line Intensities

The line intensities play a vital role for the proper identification of the observed lines. Generally, different observers use different scales to express the relative line intensities. One of the widely used techniques to provide the relative intensities is a visual assessment of the blackening of the photographic emulsion. Besides, optical densitometers are also used for this purpose. As the data under study were observed by several authors using different excitation sources and recording equipment, there was a need to convert the overall intensities to a uniform scale. This reduction was achieved by using local thermodynamic equilibrium (LTE) approximation, the detailed procedure of which has been explained in many laboratory spectrum analyses (Kramida 2013a, 2013b, 2013c; Haris et al. 2014). In this method, the effective excitation temperature for any particular atom or ion is determined using a simplified LTE model applied to the observation (line intensities). This method requires accurate transition probabilities (gA-values) as well, but they are often provided from computations. Once the approximate effective excitation temperature (T_{exc}) for the light source used has been determined, the spectral response function(s) of the instrument (including the detector) can easily be determined by comparing the observed and calculated intensities. This function is subtracted from the observed intensities to remove the effects of any spectral variations caused due to the instrument. This leads to the reduction of the corrected intensities and the obtaining of a more accurate value of T_{exc} from the Boltzmann plot. Several iterations of this procedure are performed until a reasonable convergence is

Table 1
Classified Lines of Au IV

I_{obs} [a] (arb. u.)	Char.[a]	λ_{obs} [b] (Å)	Unc.[b,c] (Å)	Lower Level[d]	Upper Level[d]	λ_{Ritz} [b] (Å)	Unc.[b] (Å)	λ_{prev}^{corr} [e] (Å)	A-value (s^{-1})[f] HFR+CPOL	A-value (s^{-1})[f] HFR	Acc.[g]	Line Ref.[h]	Comm.[i]
				$5d^8\ ^3F_4$	$5d^7(^2Da)6p\ ^1F^o_3$	524.6742	0.0008		2.51e+06	3.52e+06	E		
				$5d^8\ ^3F_4$	$5d^7(^2F)6p\ ^1F^o_3$	530.9707	0.0011		5.64e+05	5.31e+05	E		
				$5d^{83}F_4$	$5d^7(^2Db)6p\ ^3F^o_3$	535.9620	0.0009		4.87e+05	4.32e+05	E		
4900		608.188	0.005	$5d^8\ ^3P_2$	$5d^7(^2G)6p\ ^1F^o_3$	608.1802	0.0008	608.183	4.08e+07	5.88e+07	D	TW,J91	U
1800	*	608.883	0.016	$5d^8\ ^3F_4$	$5d^7(^2G)6p\ ^3F^o_3$	608.8920	0.0008	608.887	4.18e+07	3.49e+07	D	TW,J91	
1800	*	608.883	0.013	$5d^8\ ^3P_1$	$5d^7(^2Da)6p\ ^3F^o_2$	608.8844	0.0011	608.887	1.11e+08	1.40e+08	D+	TW,J91	
940		610.140	0.005	$5d^8\ ^3F_3$	$5d^7(^2P)6p\ ^3D^o_2$	610.1429	0.0008	610.143	8.61e+07	4.78e+07	D	TW,J91	
650		1110.180	0.005	$5d^7(^2F)6s\ ^3F_2$	$5d^7(^2H)6p\ ^3G^o_3$	1110.1858	0.0022		6.38e+07	8.22e+07	D+	TW	
1500		1110.657	0.005	$5d^7(^2G)6s\ ^3G_4$	$5d^7(^2G)6p\ ^1H^o_5$	1110.6593	0.0016	1110.659	8.62e+07	8.77e+07	D+	TW,W94	V
930	d	1110.872	0.010	$5d^7(^4P)6s\ ^5P_2$	$5d^7(^2Db)6p\ ^3D^o_3$	1110.8667	0.0013	1110.866	2.51e+08	2.76e+08	D+	TW,W94	
930	d	1110.951	0.010	$5d^7(^2H)6s\ ^3H_6$	$5d^7(^2H)6p\ ^3H^o_5$	1110.9557	0.0024	1110.951	1.55e+08	1.42e+08	D+	TW,W94	
480	SA	1510.878	0.005	$5d^7(^4F)6s\ ^3F_4$	$5d^7(^4F)6p\ ^5G^o_4$	1510.8796	0.0022	1510.880	1.31e+08	1.25e+08	D+	TW,W94	
480	d	1511.011	0.010	$5d^7(^4F)6s\ ^5F_1$	$5d^7(^4F)6p\ ^5F^o_2$	1511.010	0.003	1511.005	8.54e+07	1.11e+08	D+	TW,W94	
450		1511.442	0.005	$5d^7(^2P)6s\ ^3P_1$	$5d^7(^2P)6p\ ^3D^o_1$	1511.4414	0.0023	1511.443	9.90e+07	1.09e+08	D+	TW,W94	U
89		1891.924	0.005	$5d^7(^2P)6s\ ^1P_1$	$5d^7(^4F)6p\ ^5F^o_2$	1891.930	0.003	1891.928	3.80e+06	5.58e+06	D	TW,W94	T
				$5d^7(^2F)6s\ ^3F_3$	$5d^7(^4F)6p\ ^5D^o_4$	3624.831	0.013		2.42e+04	2.27e+04	E		

Notes. A few columns are omitted in this condensed sample, but their footnotes (c, d, and f) are fully retained for guidance regarding their types and content.

[a] Averaged relative observed intensities in arbitrary units are given on a uniform scale corresponding to the Boltzmann populations in a plasma with an effective excitation temperature of 5.5 eV, for our spectrum (see Section 5). The intensity value is followed by the line character, encoded as follows: bl—blended by other lines; d—diffused; h—hazy; m—masked by other nearby lines; q—asymmetric; s—shaded; SA—self-absorbed; SL—shoulder line of long-wavelength side; SS—shoulder line of short-wavelength side; w—wide; ++—more intense than expected; ?—questionable line; and *—intensity shared by more than one line.

[b] Observed and Ritz wavelengths are in vacuum for $\lambda < 2000$ Å and in standard air outside this limit. Conversion between air and vacuum was made with the five-parameter formula from Peck & Reeder (1972). Assigned uncertainty of given observed wavelengths or the computed uncertainty of the Ritz wavelengths are determined in the level optimization procedure.

[c] Observed wavenumber (in vacuum) and its uncertainty. These two columns are omitted from this condensed table.

[d] Level designations and their energies from Table 2. Two columns for energies are dropped from this condensed table.

[e] Previous observed wavelength, reported either by Joshi et al. (1991) or by Wyart et al. (1994), was corrected using the Ritz wavelength of this work (see Section 4).

[f] Transition rates or A-values, from HFR+CPOL and HFR calculations. The quantity $|CF|_{min}$ is the minimum of their absolute cancellation factors (see Section 7). This column of $|CF|_{min}$ is omitted from this condensed table.

[g] Accuracy code of the A-value is given in Table 4 (see Section 7.1).

[h] Line references: J91—Joshi et al. (1991); W94—Wyart et al. (1994); and TW—this work.

[i] Comments: T—the variation of the individual line intensities used for intensity averaging is within a factor of 1; U—those vary within a factor of 2; V—those vary within a factor of 3; W—those vary by more than a factor of 3 but less than 10; X—the variation is more than a factor of 10, hence it is excluded from the intensity averaging; Y—the line reported by the previous observer is a perturbed line, therefore it is excluded from the intensity averaging.

(This table is available in its entirety in machine-readable form.)

Table 2
Optimized Energy Levels of Au IV

Configuration[a]	Term[a]	J	Energy (cm^{-1})	Unc.[b] (cm^{-1})	Perc.[c]	Perc2[c]	Conf2[c]	Perc3[c]	Conf3[c]	NoL[d]	ΔE^{e}_{o-c} (cm^{-1})	Comm.[f]
$5d^8$	^3F	4	0.00	0.20	94	5	$5d^8\ ^1G$		...	39	131	
$5d^8$	^3P	2	6630.12	0.18	46	35	$5d^8\ ^1D$	18	$5d^8\ ^3F$	43	−63	
$5d^8$	^3F	3	12,293.66	0.18	99		...		...	40	41	
$5d^8$	^3F	2	18,100.97	0.16	48	46	$5d^8\ ^3P$		...	48	−37	
$5d^8$	^3P	0	18,185.2	0.4	82	16	$5d^8\ ^1S$		...	11	−161	
$5d^8$	^3P	1	21,489.95	0.21	97	2	$5d^7(^2P)6s\ ^3P$		...	27	−9	
$5d^8$	^1G	4	25,702.13	0.16	94	5	$5d^8\ ^3F$		...	31	33	
$5d^8$	^1D	2	30,735.67	0.20	49	35	$5d^8\ ^3F$	14	$5d^8\ ^3P$	30	−5	
$5d^7(^4F)6s$	^5F	5	51,296.97	0.15	86	13	$5d^7(^2G)6s\ ^3G$		...	12	−105	
$5d^8$	^1S	0	55,277.8	0.3	83	15	$5d^8\ ^3P$		...	6	64	N
$5d^7(^4P)6s$	^5P	3	68,890.98		67	17	$5d^7(^4F)6s\ ^5F$	8	$5d^7(^4F)6s\ ^3F$	30	39	B
$5d^7(^4P)6s$	^5P	1	72,968.57	0.09	47	24	$5d^7(^4F)6s\ ^5F$	19	$5d^7(^2P)6s\ ^3P$	21	133	
$5d^7(^2G)6s$	^3G	5	75,093.20	0.10	59	23	$5d^7(^2H)6s\ ^3H$	12	$5d^7(^4F)6s\ ^5F$	18	−165	
$5d^7(^4F)6s$	^3F	3	75,819.28	0.08	58	14	$5d^7(^4P)6s\ ^5P$	13	$5d^7(^2Db)6s\ ^3D$	30	−30	
$5d^7(^2Da)6s$	^1D	2	123,610	200	75	7	$5d^7(^2Db)6s\ ^1D$	5	$5d^7(^2F)6s\ ^3F$	0		L
$5d^7(^4F)6p$	$^5D^\circ$	4	120,217.42	0.09	42	20	$5d^7(^4F)6p\ ^5F^\circ$	13	$5d^7(^2G)6p\ ^3F^\circ$	7	104	
$5d^7(^4F)6p$	$^3G^\circ$	5	122,495.68	0.21	30	30	$5d^7(^4F)6p\ ^5F^\circ$	21	$5d^7(^4F)6p\ ^5G^\circ$	5	359	
$5d^7(^2P)6p$	$^3P^\circ$	1	130,380.25	0.10	23	12	$5d^7(^2Db)6p\ ^3D^\circ$	10	$5d^7(^4P)6p\ ^5D^\circ$	8	−145	
$5d^7(^2Da)6p$	$^1P^\circ$	1	207,500	400	50	20	$5d^7(^2Da)6p\ ^3D^\circ$	6	$5d^7(^2Db)6p\ ^3P^\circ$	0		L
$5d^7(^2Da)6p$	$^3D^\circ$	3	207,800	400	46	16	$5d^7(^2Db)6p\ ^3D^\circ$	15	$5d^7(^2Da)6p\ ^1F^\circ$	0		L

Notes.
[a] The level designations are in the LS coupling scheme. Designations in "Configuration" and "Term" may correspond to a component with the second-/third-/fourth-largest percentage in the eigenvector and they are opted to uniquely define the levels (see the text).
[b] The quantity given in the "Unc." column is the uncertainty of separation from the "base" level $5d^7(^4P)6s\ ^5P_3$ at 68,890.98 cm^{-1} (see Section 4). To estimate the uncertainties of excitation energies from the ground level, the given values in the "Unc." column should be combined in quadrature with the uncertainty of the ground level, 0.20 cm^{-1}. All uncertainties are derived by the LOPT code.
[c] The first leading percentage value refers to the configuration and term given in the first two columns of the table. The second, third, fourth, and fifth percentages refer to the configuration and term subsequent to them. The four columns (for the fourth and fifth percentages and their compositions) are omitted from this condensed table.
[d] Number of observed lines determining the level in the level optimization procedure. Zero for unobserved levels.
[e] Differences between the energy observed and those calculated in the parametric LSF with Cowan's code. Blank for unobserved levels.
[f] Comments: B—the base level for presentation of uncertainties; L—the level position and its uncertainty are obtained in the parametric LSF calculations with Cowan's codes; N—new level; and R—revised level.

(This table is available in its entirety in machine-readable form.)

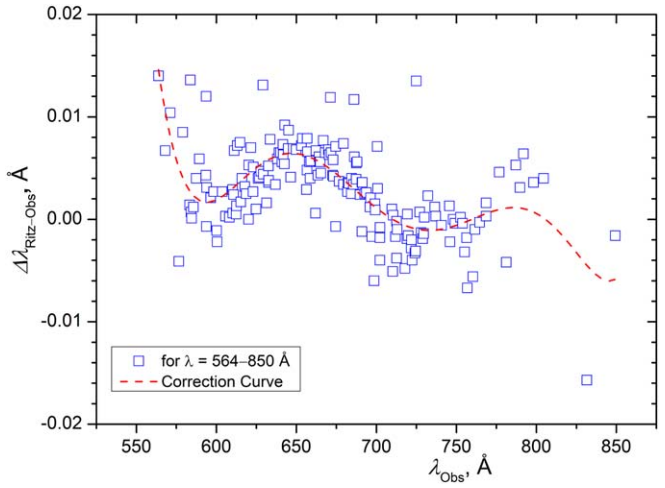

Figure 1. Comparison of wavelengths observed by Joshi et al. (1991) with those of Ritz in this work. The dashed line represents a correction curve fitted with a seventh-order polynomial function (see the text).

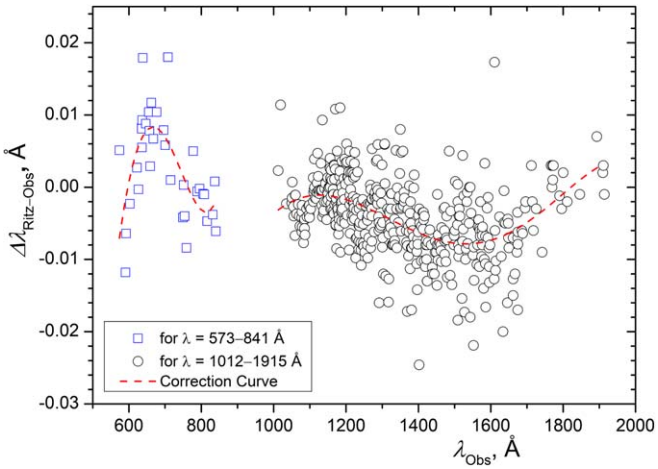

Figure 2. Comparison of wavelengths observed by Wyart et al. (1994) with those of Ritz in this work. The dashed lines represent the correction curves—the first ($\lambda < 1000$ Å) is fitted with a fourth-order polynomial and the second is made with a fifth-order polynomial function (see the text).

reached. In the same manner, T_{exc} is derived for each set of observations. Finally, all of them were effectively reduced to a global uniform scale with a common T_{exc} obtained from one of the observations. If the same set of observed lines is available from multiple sources, the modeled intensities for each of them are averaged out.

The abovementioned procedure was followed for the intensities of Au IV lines observed on our spectrograms, which were taken from seven different plates recorded at different

experimental conditions on the same instrument. It should be noted that our originally recorded intensities are visual estimates of the photographic blackening of emulsion. The modeling of the intensities was done using the weighted transition rates obtained from HFR+CPOL calculations. The final T_{exc} for the light source used for the present study was derived to be 5.5 eV. This temperature was chosen as the base to reduce the intensities of other observations (Joshi et al. 1991; Wyart et al. 1994).

Joshi et al. (1991) measured the relative positions of the observed lines on a Cospinsca or Grant semiautomatic comparator and reported the intensity on a scale of 1 to 99. On the other hand, the intensities reported by Wyart et al. (1994) were obtained mostly from a densitometer, which they traced for four separate spectral plates. For a few sets of lines the visual estimates were also made. Wyart et al. (1994) mentioned that the comparisons of the line intensities were limited to a small span of wavelength range, and the intensities were not consistent for the entire range of observation. They also supplemented the line list with the gold plates recorded on the same experimental setup as Joshi et al. (1991). To reduce these (Joshi et al. 1991; Wyart et al. 1994) relative intensities into a common T_{exc} scale, we combined their observations and a $T_{exc} = 5.3$ eV was obtained for the combined observation. To compare (and to average) these line intensities with those of our spectrograms, the reduced (corrected) intensities were further scaled with respect to the common $T_{exc} = 5.5$ eV of our work. In the end, the modeled line intensities for the commonly observed lines were compared, and an averaging of them was made if they agreed within a standard deviation of one order of magnitude. Our final modeled line intensities with their line characters ("I_{obs}" and "Char.") are given in the first two columns of Table 1, and the lines particularly excluded from the intensity averaging, marked with the "X" symbol, are given in the last column of the same table.

6. Theoretical Interpretation

To obtain theoretical support for our experimental findings, the theoretical calculations for energy levels, wavelengths, and transition rates (A-values) of Au IV were performed using Cowan's codes (Cowan 1981). This atomic structure calculation code works on the formalism of the pseudorelativistic HFR method with the superposition of interacting configurations. However, it has been shown recently (Quinet et al. 2006; Xu et al. 2007) that inclusion of CPOL is significantly important to achieve accurate theoretical radiative lifetimes (or transition rates) for the Os I isoelectronic sequence. This motivated us to perform a new set of improved HFR+CPOL calculations.

To obtain the radiative lifetime data for the levels of $5d^8$ and $5d^7 6s$ configurations, in addition to HFR and HFR+CPOL calculations, separate computations were also made with a fully relativistic multiconfiguration Dirac–Hartree–Fock (MCDHF) method (Grant 2007; Froese Fischer et al. 2016) implemented in the latest version of the General Relativistic Atomic Structure Program, namely GRASP2018 (Froese Fischer et al. 2019).

Further details of these individual calculations are described in the subsections below. The results and discussion of the critical evaluation of the transition rate data produced by different theoretical methods are given in Section 7.

6.1. The HFR Calculations

Our extensive HFR calculations contain all major interacting configurations for both parities. The even parity set consists of $5d^8$, $5d^7ns$ (n = 6–8), $5d^7nd$ (n = 6–8), $5d^6 6l^2$ ($l = s, p$), $5d^6 6s6d$, and $5d^6 6s7s$ configurations, whereas $5d^7np$ (n = 6–8), $5d^7nf$ (n = 5–7), $5d^6 6snp$ (n = 6, 7), and $5d^5 6s^2 6p$ configurations were included in the odd parity system. The initial scaling for the average energy (E_{av}) and spin–orbit interaction (ζ_{nl}) parameters was kept at 100% of the HFR values, while the radial wave integral (F^k), exchange integral (G^k), and configuration interaction integral (R^k) were fixed at 75% of the HFR values. A parametric least-squares fitting (LSF) was performed to minimize the differences between the observed and theoretical energy level values. The standard deviations of the LSF calculations for the even and odd parity systems were found to be 92 cm^{-1} and 176 cm^{-1}, respectively. The fitted LSF parameters are shown in Table 3 and were further used to compute the improved transition parameters.

6.2. The HFR+CPOL Calculations

The physical model used for the HFR+CPOL calculations is based on the consideration of valence–valence (VV) correlations within a set of interacting configurations, including $5d^8$, $5d^7ns$ (n = 6–8), $5d^7nd$ (n = 6–8), $5d^6 6s^2$, $5d^6 6p^2$, $5d^6 6d^2$, $5d^6 6s6d$, $5d^6 6s7s$ and $5d^7$ np (n = 6–8), $5d^7$ nf(n = 5–6), $5d^6 6snp$ (n = 6–7), $5d^6 6p6d$, $5d^6 6s5f$ for even and odd parities, respectively. This list of configurations includes a large amount of valence correlation outside the W-like Au VI ionic core. Therefore, we estimated the core–valence (CV) interactions by considering CPOL contributions with the dipole polarizability, α_d, equal to 3.62 a_0^3, and a cutoff radius, r_c, equal to 1.40 a_0. As no data are available in the literature, the first parameter was deduced from the extrapolation of α_d-values published by Fraga et al. (1976) along the tungsten isoelectronic sequence, from W I to Pt V. As for the cutoff radius, it corresponds to the HFR average value $\langle r \rangle$ for the outermost core orbital ($5d$). The semi-empirical LSF approach performed using this HFR +CPOL model gave similar results to those obtained in our HFR calculations, with standard deviations of 111 cm^{-1} and 173 cm^{-1} in even and odd parities, respectively.

6.3. The MCDHF Calculations

The MCDHF calculations are based on two multireferences (MRs) for even and odd parities, including the $5d^8$, $5d^7 6s$, $5d^6 6s^2$, $5d^7 6p$, and $5d^6 6s6p$ configurations, respectively. The orbitals were optimized using all the energy levels from each MR. VV correlations were estimated by considering single and double (SD) excitations from the MR configurations to $7s$, $7p$, $7d$, and $7f$ orbitals, giving rise to 143,441 and 602,493 configuration state functions (CSFs) in the even and odd parities, respectively. In this step, only the new orbitals were optimized, the other ones being kept to their values obtained before. Then CV effects were taken into account, by considering SD excitations from the $4d$, $4f$, $5s$, and $5p$ core orbitals to the valence orbitals characterizing the MR configurations. This led to 344,673 CSFs (even parity) and 623,038 CSFs (odd parity). The electric dipole (E1) transitions, allowing us to estimate the MCDHF radiative lifetimes of Au IV levels, were computed by gathering the two parities, while the transition probabilities for forbidden lines (M1 and E2) were considered only within the even parity.

Table 3
LSF Parameters for Au IV

Configuration[a]	Slater Parameter[a]	LSF[a] (cm^{-1})	Unc.[b] (cm^{-1})	Index[c]	HFR[a] (cm^{-1})	LSF/HFR[a]	Comments[d]
$5d^8$	E_{av}	18,247.6	37.0		19,163.7	0.952	
$5d^8$	$F^2(5d, 5d)$	59,636.9	157.0	1	73,337.2	0.813	
$5d^8$	$F^4(5d, 5d)$	44,803.0	275.0	2	48,865.2	0.917	
$5d^8$	$\alpha(5d)$	17.2	4.0	3	0.0		
$5d^8$	$\beta(5d)$	−437.9	−74.0	7	0.0		
$5d^8$	$T(5d)$	0.0			0.0		F
$5d^8$	$\zeta(5d)$	5589.7	16.0	4	5769.1	0.969	
$5d^7 6s$	E_{av}	85,932.6	20.0		89,638.1	0.959	
...	R^k					0.750	R
$5d^7 6p$	E_{av}	164,844.4	21.0		166,636.7	0.989	
$5d^7 6p$	$F^2(5d, 5d)$	60,028.6	247.0	1	75,500.9	0.795	
$5d^7 6p$	$F^4(5d, 5d)$	44,375.0	473.0	2	50,491.4	0.879	
$5d^7 6p$	$\alpha(5d)$	21.9	4.0	3	0.0		
...	R^k					0.750	R

Notes.
[a] Configurations involved in the calculations and their defining Slater parameters with their HFR and/or LSF value or their ratio.
[b] Uncertainty of each parameter represents the standard deviation. Blank for fixed values.
[c] Parameters in each numbered group were linked together with their ratio fixed at the HFR level.
[d] Comments: F—the parameters are fixed at a given LSF/HFR ratio; and R—all configuration interaction parameters R^k in both even and odd parity sets are fixed at 75% of their HFR value.

(This table is available in its entirety in machine-readable form.)

7. Evaluation of Transition Rates

An energy level diagram for the known levels of Au IV is illustrated in Figure 3, along with its intra- and inter-configuration transitions. In terms of the observations, only the allowed electric dipole E1 types of ($5d^8$ + $5d^7 6s$)–$5d^7 6p$ transitions are observed (see Table 1). The forbidden M1-type (magnetic dipole) radiations are dominant in the intraconfiguration transitions, for example, within the levels of the $5d^8$ and $5d^7 6s$ configurations. However, in the case of the $5d^8$–$5d^7 6s$ interconfiguration transitions, the transition amplitudes are largely forbidden E2 types (electric quadrupole).

For E1 types, the transition rates (A-values) were obtained from the HFR and HFR+CPOL methods, and their comparisons are described in Section 7.1. On the other hand, for forbidden M1 and E2 types, the transition parameters including A-values were obtained from three different methods (namely: MCDHF, HFR, and HFR+CPOL), and their comparisons are discussed separately, in Section 7.2.

7.1. Allowed E1-type Transitions

As discussed briefly above, the inclusion of CPOL effects in HFR calculations significantly improves the accuracy of the transition rate data (or lifetime $\tau_k = 1/\Sigma A_{ki}$ data) for Os I and Ir II (Quinet et al. 2006; Xu et al. 2007). These authors have shown that their computed lifetime data from the HFR+CPOL calculations agree fairly well (within 30% and 20% for Os I and Ir II, respectively) with the experimental lifetime data (for 10 available levels of the $5d^7 6p$ configuration). No experimental lifetime data are available for higher members of the Os I sequence, including the Au IV spectrum. Nonetheless, comparison of the transition rates from different sources is a prerequisite to estimate the uncertainty of the transition rate data (Kramida 2013a; Haris et al. 2014). The computed lifetime data for the levels of $5d^7 6p$ from the HFR calculations are systematically (about 73%) lower than those of the HFR+CPOL ones. Therefore, the HFR lifetime data are scaled to the HFR+CPOL level, and using the scaled lifetime data, the HFR transition rates were recalculated. For comparison, the transition rates are first converted into their corresponding "line strengths" (S-values) using the numerical expression $S = gA\lambda^3/2.0261269\text{e}{+18}$, where line strength S (in atomic units,

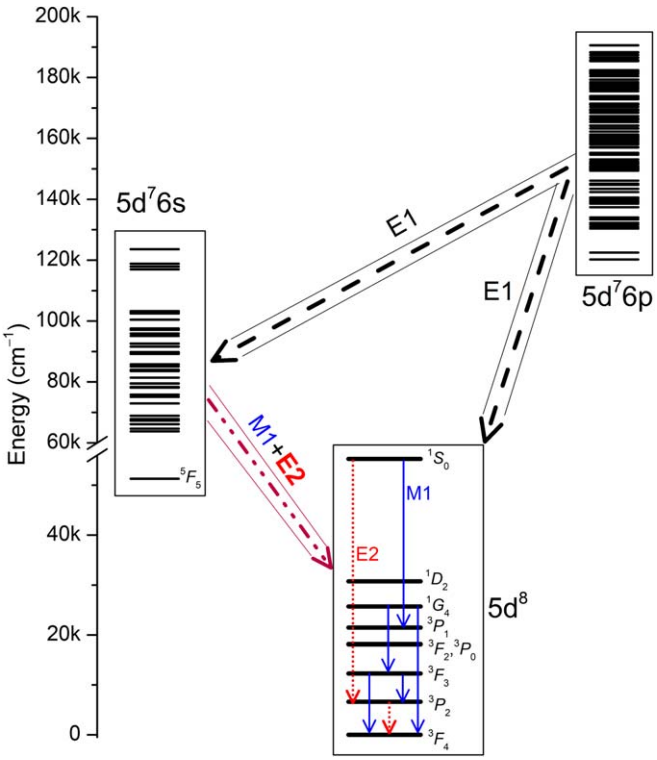

Figure 3. Energy level diagram for the known levels of Au IV. Fine structure levels of the ground $5d^8$ configuration are shown, along with their selected forbidden (M1 and E2) transitions. The transitions within the levels of $5d^7 6s$ are not shown.

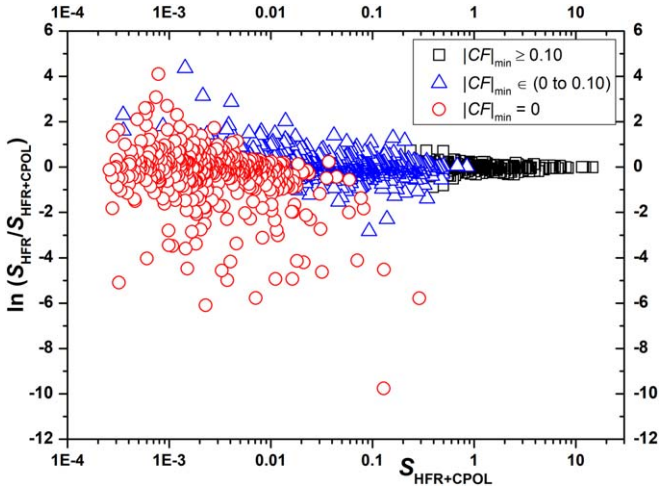

Figure 4. Comparison of line strengths (*S*-values) computed within the framework of the HFR and HFR+CPOL calculations for E1 types. For the uncertainty evaluations, the entire data were divided into three separate groups, depending on their $|CF|_{min}$ values (see the text).

AU), weighted transition rate gA (in s^{-1}), and wavelength λ (in Å) are expressed in their customary units. The logarithmic difference of the two sets of *S*-values (HFR and HFR+CPOL) as a function of $S_{HFR+CPOL}$ is plotted and is shown in Figure 4. It is evident from Figure 4 that the uncertainty varies with the *S*-values, but apart from the dependency on magnitude of the S-value, it also depends on the absolute value of the cancellation factor (CF) (Cowan 1981). Both HFR and HFR +CPOL calculations provide the CF factor, thus a minimum value, $|CF|_{min}$, is taken into account. Generally, the *S*-values (or transition rates) with $|CF| < 0.10$ are considered as unreliable (Kramida 2013a), but we found that the average deviation of *S*-values with $0 < |CF|_{min} < 0.10$ is about 62% and those with $|CF|_{min} = 0$ deviate by more than three orders of magnitude. In fact, the lines with $|CF|_{min} \geqslant 0.10$ show the least deviation or they have a higher accuracy. The uncertainty evaluations are made separately for three different cases of $|CF|_{min}$ and the results are summarized in column (2) of Table 4. It should be noted that these uncertainties represent the statistical ($Unc._{stat}$) ones for the two data sets, and for more comprehensive uncertainty estimates, experimental lifetime data and their agreement with the theoretical data are required. Since no experimental lifetime data are available for Au IV, a conservative estimate of additional (systematic) uncertainty of about 30% was adopted from the Os I and Ir II lifetime data comparisons, as discussed above. To derive the final total uncertainties ($Unc._{tot}$) for *A*-values, the systematic uncertainty is combined in quadrature with $Unc._{stat}$, and their corresponding uncertainty codes are provided in Table 1.

7.2. Forbidden M1- and E2-type Transitions

In this section, a comparative evaluation of the *A*-values for the forbidden transitions, within the levels of $5d^8$ and $5d^76s$ and those of $5d^8$–$5d^76s$, from three different computational approaches, namely MCDHF, HFR, and HFR+CPOL, has been presented. For comparison purposes, the initially obtained *A*-values from these sources were first normalized or rescaled with respect to the experimental transition energies, which are computed from Table 2. These *A*-values were also used to compute the radiative lifetimes for the levels of $5d^8$ and $5d^76s$ configurations, and these lifetimes are given in Table 5.

Table 4
Uncertainty Estimates and Codes for Transition Rates of Allowed (E1) and Forbidden (M1 + E2) Types

$Unc._{stat}$ for E1 Type[a]		$Unc._{tot}$[b]		
$S_{HFR+CPOL}$ (AU)	$Unc._{stat}$	Symbol	In *A*-value	In log(*gf*)
…	…	C	⩽25%	⩽0.11
(i) For $\|CF\|_{min} \geqslant 0.10$				
⩾2	10%	D+	⩽40%	⩽0.18
[0.2, 2)	17%	D+	⩽40%	⩽0.18
(ii) For $\|CF\|_{min} < 0.10$				
[0.2, 0.9)	25%	D+	⩽40%	⩽0.18
[0.02, 0.2)	35%	D	⩽50%	⩽0.24
[0.002, 0.02)	50%	E	>50%	>0.24
(iii) For $\|CF\|_{min} = 0$				
<0.002	300%	E	>50%	>0.24

Notes.
[a] The statistical uncertainty ($Unc._{stat}$) is estimated from the comparison of two (HFR and HFR+CPOL) data sets.
[b] The total uncertainty ($Unc._{tot}$) includes an additional 30% of the systematic component, combined in quadrature with $Unc._{stat}$ for all E1 types (see Section 7.1). For forbidden (M1 + E2) types, the $Unc._{tot}$ is determined from the comparison of different data sets (see Section 7.2).

The evaluations were started with comparisons of the HFR and HFR+CPOL results for M1- and E2-type transitions, which are shown in Figure 5. The error bars in this figure represent the internal uncertainties of the *S*-values obtained from the HFR calculations, which have been evaluated using the Monte Carlo technique (Kramida 2014). A total of 20 trials were made to estimate the uncertainties (of *A*- or *S*-values) for 537 M1- and 777 E2-type transitions. About 835 transitions have their uncertainty within 3%, 238 transitions have 7%, 132 have 18%, 61 transitions have uncertainties varying between 25% and 50%, and 48 transitions have more than 50% (half of them have deviations of two or three orders of magnitude). In general, an excellent agreement (within 0.33 dex) is observed for HFR and HFR+CPOL data sets: as expected, the strong lines with *S* (in AU) ⩾1 agreed within 10% of the uncertainty, 18% for the lines with $S \in [0.2, 1)$, 25% for $S \in [0.02, 0.2)$, 40% for $S \in [0.0001, 0.02)$, and the remaining weak lines deviated by more than 50%.

However, in order to obtain more reliable estimates, the *S*-values from HFR and HFR+CPOL were further compared with the MCDHF ones. For M1 types of transitions, the S_{MCDHF}-values agree within 0.79 dex and 0.68 dex for S_{HFR} and $S_{HFR+CPOL}$, respectively. In the case of E2 types, the S_{MCDHF}-values are available in length and velocity (Babushkin and Coulomb gauges, respectively) forms. Comparison of these two forms reflects the internal accuracy of the computation, which is generally given in terms of the uncertainty indicator δT, defined as $\delta T = |A^l - A^v|/\max(A^l, A^v)$, where A^l and A^v are the A_{ki}-values calculated in length and velocity gauges, respectively. Note that a similar indicator, δS, can also be computed from their corresponding *S*-values. However, using δT or δS for the computation of uncertainty is normally discouraged, since the presence of the "max" term in the denominator underestimates the uncertainty

Table 5
Radiative Lifetimes τ (in Milliseconds) for the Levels of $5d^8$ and $5d^7 6s$ in Au IV

Level[a]	ΔE_{O-M} [b] (cm^{-1})	MCDHF[c] τ^v	MCDHF[c] τ^l	HFR+CPOL[c] τ
$5d^8\ ^3F_4$	0	...	...	...
$5d^8\ ^3P_2$	−1157	2284000	1136000	891000
$5d^8\ ^3F_3$	810	21.00	21.00	21.27
$5d^8\ ^3F_2$	−307	38.1	37.9	37.9
$5d^8\ ^3P_0$	−2101	930000	12130	11430
$5d^8\ ^3P_1$	−1491	44.1	44.1	36.5
$5d^8\ ^1G_4$	−2330	45.8	46.1	34.4
$5d^8\ ^1D_2$	391	10.57	10.54	9.12
$5d^7(^4F)6s\ ^5F_5$	2426	65.2	117.8	105.8
$5d^8\ ^1S_0$	−2001	3.21	2.90	2.60
$5d^7(^4F)6s\ ^5F_4$	2310	8.41	12.59	8.47
$5d^7(^4F)6s\ ^5F_3$	2598	28.9	31.2	26.8
$5d^7(^4P)6s\ ^5P_2$	1756	9.80	10.59	7.41
$5d^7(^4F)6s\ ^5F_1$	1937	9.21	11.89	8.58
$5d^7(^4F)6s\ ^5F_2$	1289	7.45	8.99	14.70
$5d^7(^4F)6s\ ^3F_4$	1420	1.147	1.595	1.684
$5d^7(^4P)6s^5P_3$	1142	7.69	9.15	9.58
$5d^7(^4P)6s\ ^5P_1$	1219	6.06	7.86	9.31
$5d^7(^2G)6s\ ^3G_5$	754	1.812	2.456	2.211
$5d^7(^4F)6s\ ^3F_3$	1301	1.116	1.443	1.304
$5d^7(^4F)6s\ ^3F_2$	1094	1.142	1.502	1.373
$5d^7(^2G)6s\ ^3G_4$	630	1.840	2.59	2.130
$5d^7(^2P)6s\ ^1P_1$	640	1.139	1.404	1.315
$5d^7(^4P)6s\ ^3P_2$	511	0.839	0.969	0.900
$5d^7(^2H)6s\ ^3H_6$	−536	1.394	2.097	1.779
$5d^7(^2P)6s\ ^3P_0$	471	1.493	1.934	1.475
$5d^7(^2G)6s\ ^3G_3$	919	2.207	2.92	2.84
$5d^7(^2H)6s\ ^3H_5$	−634	1.869	2.92	2.477
$5d^7(^2G)6s\ ^1G_4$	5	1.196	1.675	1.482
$5d^7(^2Db)6s\ ^3D_3$	1934	1.045	1.205	1.117
$5d^7(^2Db)6s\ ^3D_2$	858	0.833	1.049	1.080
$5d^7(^4P)6s\ ^3P_1$	1216	0.879	0.969	0.987
$5d^7(^2F)6s\ ^3F_2$	845	1.036	1.164	1.560
$5d^7(^2P)6s\ ^3P_2$	−1311	1.807	2.352	1.142
$5d^7(^2F)6s\ ^3F_3$	−2262	1.250	1.566	1.242
$5d^7(^2P)6s\ ^3P_1$	1190	1.216	1.432	1.399
$5d^7(^2H)6s\ ^3H_4$	286	1.358	1.861	1.733
$5d^7(^2H)6s\ ^1H_5$	−273	0.870	1.250	1.095
$5d^7(^4P)6s\ ^3P_0$	995	0.537	0.608	0.603
$5d^7(^2F)6s\ ^3F_4$	−926	1.205	1.538	1.181
$5d^7(^2Db)6s\ ^1D_2$	−531	0.780	0.915	0.788
$5d^7(^2Db)6s\ ^3D_1$	−482	0.846	0.996	0.836
$5d^7(^2F)6s\ ^1F_3$	−1945	0.661	0.787	0.739
$5d^7(^2Da)6s\ ^3D_1$	250	0.678	0.661	0.566
$5d^7(^2Da)6s\ ^3D_2$	−162	0.638	0.647	0.546
$5d^7(^2Da)6s\ ^3D_3$	−2517	0.633	0.648	0.525
$5d^7(^2Da)6s\ ^1D_2$	−2292	0.425	0.432	0.374

Notes.
[a] The levels are from Table 2.
[b] Difference between the observed energy level value and its corresponding MCDHF value in cm^{-1}.
[c] The MCDHF (in velocity and length forms) and HFR+CPOL radiative lifetimes (in milliseconds) for the levels were determined using the scaled A-values. The scaling was carried out with the help of transition energies computed from Table 2 (see the text).

(Kramida et al. 2022b). Instead a reliable uncertainty estimate can be obtained from the dS comparisons, which are made as a function of S-values (see Section 7.1). For the present case, the global disagreement, between length and velocity forms, for 777 E2-type transitions is within 1.22 dex or three orders of magnitude. However, this large deviation does not necessarily means the entire computational accuracy is poorer, as the stronger S-values of a certain type of transition still have better agreement. As E2 types are dominant for interconfiguration transitions, they ought to have better accuracy. This can be confirmed from the gross deviation for the $5d^8$–$5d^7 6s$ transitions, which is ≈0.44 dex and ≈1.4 dex for the transitions within the levels of the $5d^8$ and $5d^7 6s$ configurations. Both length and velocity forms should produce comparable results with reasonably accurate approximate wave functions, yet the velocity forms are not a good choice for small transition energies (Cowan 1981). Therefore, in general, length form results are considered to be more accurate than those of velocity form (Hibbert 1974; Froese Fischer 2009), except in the case of the Rydberg type of transitions, for which velocity forms could be more appropriate (Papoulia et al. 2019).

For this reason, we have chosen the length form for the final comparisons. The agreement of the $S_{\rm MCDHF}$-values for E2-type transitions is ≈0.80 dex with $S_{\rm HFR}$ as well as with $S_{\rm HFR+CPOL}$-values. The comparison plots of M1 and E2 types for HFR+CPOL and MCDHF calculations are shown in Figure 6, which represent a fairly good agreement, since their gross deviation was within 0.68 dex and 0.80 dex, respectively. For M1-type transitions, the strong lines with S (in AU) $\geqslant$2 agreed within 25% of uncertainty, 38% for the lines with $S \in [0.6, 2)$, 50% for $S \in [0.1, 0.6)$, and the remaining weak lines are deviated by more than 50%. Similarly for E2 transitions, lines with $S \geqslant 5$ agreed within 23%, 40% for the lines with $S \in [1, 5)$, 50% for $S \in [0.3, 1)$, and the rest of the weak lines are deviated by more than 50%. The data on the transition rates (A-values) of the M1 and E2 components, obtained from MCDHF, HFR+CPOL, and HFR calculations, along with their accuracy codes and absolute branching fractions, are summarized in Table 6. The absolute branching fraction, $\mathrm{BF}_{ki}^{\rm abs}$, of a spectral line originating from an upper level k to a lower level i is defined as $\mathrm{BF}_{ki}^{\rm abs} = \tau_k A_{ki}^{\rm tot}$, where $A_{ki}^{\rm tot} = A_{ki}^{M1} + A_{ki}^{E2}$, and is helpful for line identification and confirmation. To derive the effective uncertainty for the $A_{ki}^{\rm tot}$ of a spectral line, its M1- and E2-component uncertainties can be directly weighted on the basis of their relative branching factor. It should be noted that our synthesized forbidden spectrum of Au IV falls in the broad wavelength range 809 Å–6.8 μm, and its numerous lines are within the bandpass of the Near Infrared Spectrograph (0.6–5 μm) and/or the Mid-Infrared Instrument (5–28 μm) of JWST. However, only a few selected strong lines of Au IV will be detected by JWST at its maximum resolution R = 3000, and all those strong lines have already been predicted by Taghadomi et al. (2022). Further, Taghadomi et al. (2022) reported transition parameters for 14 M1-type lines between the levels of $5d^8$, which we accessed from their opacity database (Stancil et al. 2021). However, our comparison shows that their disagreement was about 200% with our MCDHF and HFR+CPOL and/or HFR results. On the other hand, the agreement between our MCDHF and HFR+CPOL or HFR values was within 20% for these lines. This indicates higher computational accuracy for our results.

Finally, the lifetime data computed within the framework of the HFR, HFR+CPOL, and MCDHF calculations (see Table 5) were compared. The very close agreement, within 4%, between lifetimes from the HFR and HFR+CPOL methods should not

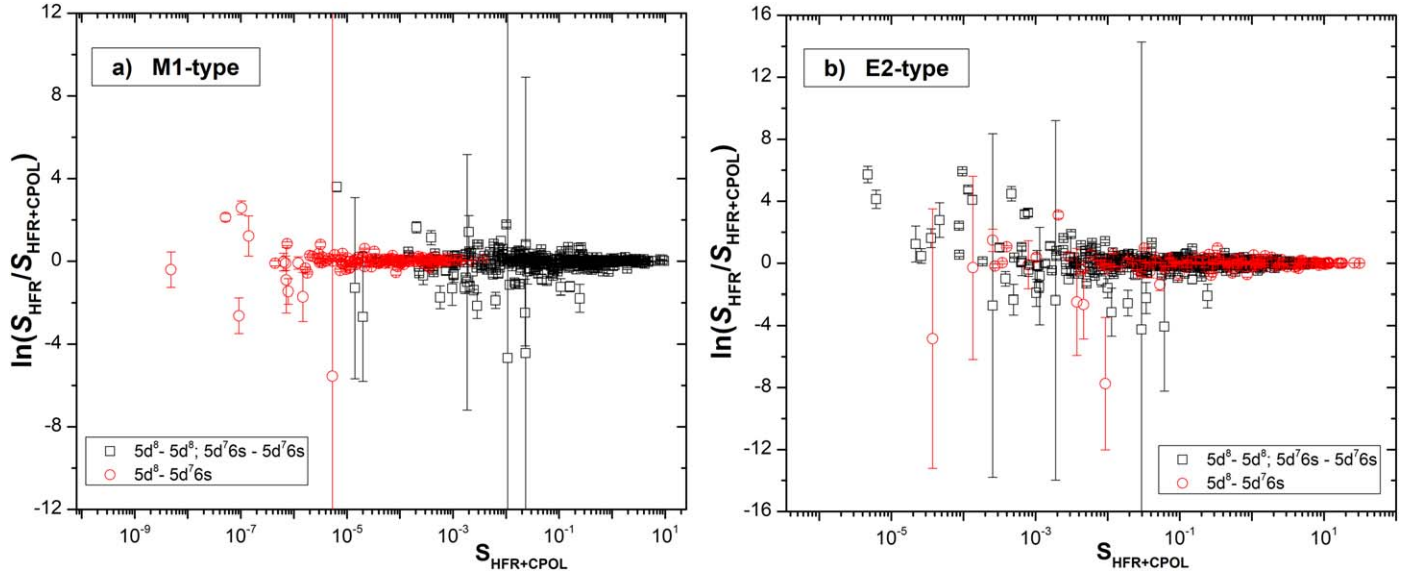

Figure 5. Comparisons of line strengths (S-values) computed within the framework of the HFR and HFR+CPOL methods for the intra- and inter-configuration transitions (see the text).

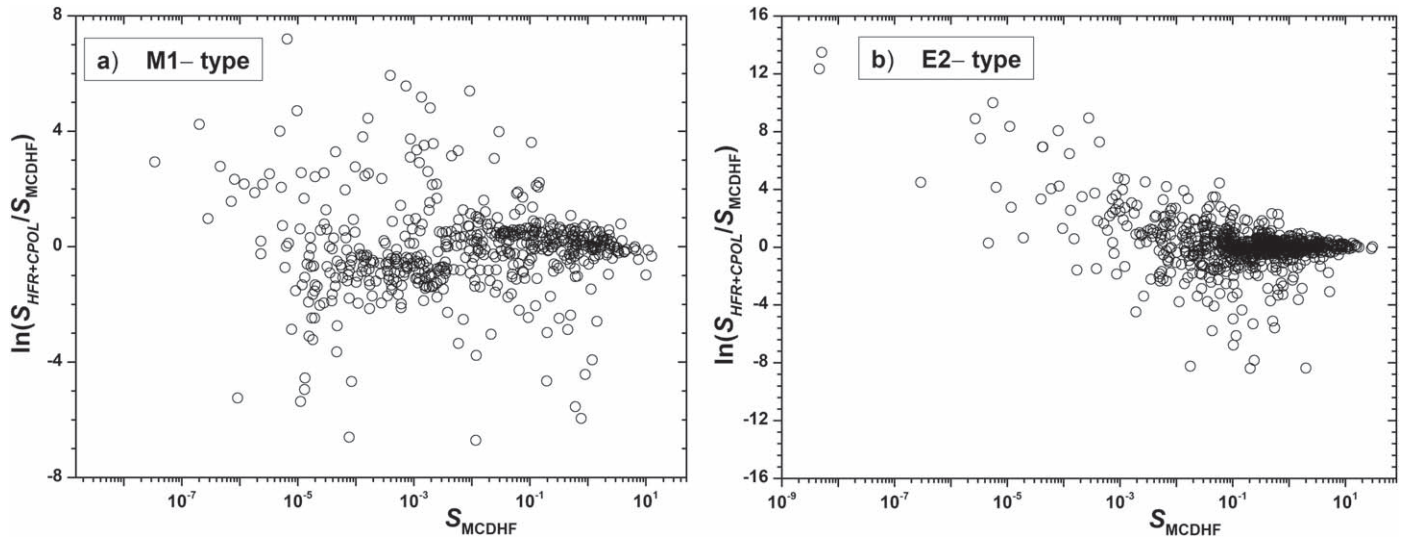

Figure 6. Logarithmic difference between the line strengths (S) from MCDHF and HFR+CPOL calculations plotted as a function of $S_{\rm MCDHF}$-values (see the text).

be overlooked. Nevertheless, the HFR+CPOL results are preferred, because they are more extensive than the other. In the MCDHF framework, the lifetime data are provided in both length and velocity forms. For the present case, their disagreement is within 30% on average, excluding those of the $5d^8\ ^3P_0$ level. This indicates that the internal consistency between length and velocity forms, even for strong branches of several transitions, is not very reliable. Most of them are interconfiguration transitions (E2 types) from the $5d^7 6s$ configuration. Finally, lifetime data from HFR+CPOL are compared with those of MCDHF. It was found that the average deviation of $\tau_{\rm HFR+CPOL}$ was 24% with respect to τ^l (length form) and 32% with respect to τ^v (velocity form). The radiative lifetime data for the levels of $5d^8$ and $5d^7 6s$ are presented in Table 5. For the computed lifetime of the uppermost $5d^7 6s\ ^1D_2$ level, at 123,610 cm^{-1}, its A_{ki}^{E1} to two lower levels of $5d^7 6p$ is not included. These transitions are allowed, but are of high-spin changing intercombination types, and hence they are very weak.

8. Transition Data of Au IV for the Calculation Opacity in Kilonova Spectra

As briefly mentioned in the introduction, Tanaka et al. (2020) and Taghadomi et al. (2022) have provided large-scale atomic data for Au IV, with specific application to compute the opacity in the kilonova ejecta. On the other hand, our results in Tables 1, 2, and 6 describe accurate Ritz wavelengths along with their transition probabilities, optimized energy levels with their uncertainties for $5d^8$, $5d^7 6s$, and $5d^7 6p$ configurations, and accurately computed line parameters for several forbidden transitions for levels of $5d^8$ and $5d^7 6s$ configurations. The accurate atomic data are important for abundance estimates of r-process elements in kilonova ejecta (Vieira et al. 2023). In their HULLAC code calculations, Tanaka et al. (2020) and Kato et al. (2021) included a limited set of configurations—namely $5d^8$, $5d^7 nl (n \geqslant 7, l = s, p)$, $5d^7 6d$, and $5d^6 6s^2$—but they generated about 30,000 E1-type transitions for their possible 507 levels, whereas Taghadomi et al. (2022) performed the

Table 6
Transition Rates for Forbidden M1 and E2 Transitions of Astrophysical Interest in Au IV

λ_{Ritz}[a] Å	Unc.[a] Å	Lower Level[b]	Upper Level[b]	A (in s^{-1}) for M1 Component[c]				A (in s^{-1}) for E2 Component[c]				BF_{abs}[e]
				MCDHF	HFR+CPOL	HFR	Acc.[d]	MCDHF	HFR+CPOL	HFR	Acc.[d]	
809.0	1.3	$5d^8\ ^3F_4$	$5d^7(^2Da)6s\ ^1D_2$					1.83e+01	1.80e+01	2.14e+01	E	0.0079
841.5	1.4	$5d^8\ ^3F_4$	$5d^7(^2Da)6s\ ^3D_3$	2.50e-01	3.81e-02	5.17e-02	E	1.85e+02	1.40e+02	1.91e+02	D	0.1197
848.1	1.4	$5d^8\ ^3F_4$	$5d^7(^2Da)6s\ ^3D_2$					3.70e+01	2.30e+01	3.36e+01	E	0.0239
854.8	1.5	$5d^8\ ^3P_2$	$5d^7(^2Da)6s\ ^1D_2$	1.69e-01	1.42e-02	1.02e-02	E	2.31e+01	5.89e+00	1.07e+01	E	0.0100
1659.480	0.004	$5d^8\ ^3F_2$	$5d^7(^2G)6s\ ^3G_4$					2.88e+01	4.22e+01	4.16e+01	D+	0.0745
1664.022	0.005	$5d^8\ ^1G_4$	$5d^7(^2G)6s^1G_4$	2.71e-01	6.05e-02	6.15e-02	E	1.23e+02	1.15e+02	1.15e+02	C	0.2073
1665.680	0.004	$5d^8\ ^3F_2$	$5d^7(^4F)6s\ ^3F_2$	7.08e-01	8.50e-02	1.12e-01	E	2.54e+01	2.38e+01	2.74e+01	D+	0.0393
1668.021	0.010	$5d^8\ ^3P_0$	$5d^7(^4F)6s\ ^3F_2$					2.97e+01	5.38e+01	4.27e+01	D+	0.0447
3222	21	$5d^7(^2P)6s\ ^3P_2$	$5d^7(^2Da)6s\ ^1D_2$	4.76e+01	2.48e+01	1.79e+01	D	2.79e-04	4.04e-01	4.79e-01	E	0.0205
3228	21	$5d^7(^2F)6s\ ^3F_3$	$5d^7(^2Da)6s\ ^1D_2$	1.82e+01	1.78e+01	2.05e+01	D	5.25e-03	7.67e-02	1.36e-01	E	0.0079
3228.761	0.013	$5d^7(^4F)6s\ ^5F_4$	$5d^7(^2Db)6s\ ^3D_3$	5.47e+01	4.15e+01	4.09e+01	D	2.98e-02	2.61e-02	2.25e-02	E	0.0660
3252.61	0.03	$5d^8\ ^3F_4$	$5d^8\ ^1D_2$					3.06e-01	2.16e-01	2.18e-01	D	0.0032
7455.92	0.13	$5d^8\ ^3F_3$	$5d^8\ ^1G_4$	1.76e+00	2.38e+00	2.37e+00	D	5.06e-06	1.02e-04	1.02e-04	E	0.0814
7467.85	0.06	$5d^7(^4F)6s\ ^5F_1$	$5d^7(^4P)6s\ ^3P_2$	6.98e+00	1.00e+01	9.56e+00	D	3.05e-03	2.79e-03	3.27e-03	D	0.0068
7467.93	0.04	$5d^7(^4F)6s\ ^3F_3$	$5d^7(^2Db)6s\ ^3D_3$	8.11e+00	9.29e+00	8.61e+00	D+	3.40e-05	2.71e-05	1.37e-05	E	0.0098
7484.56	0.06	$5d^7(^2Db)6s\ ^3D_2$	$5d^7(^2Db)6s\ ^3D_1$	1.78e+01	1.60e+01	1.71e+01	D+	2.81e-03	3.07e-03	3.20e-03	E	0.0177
12,755.91	0.17	$5d^7(^2P)6s\ ^3P_1$	$5d^7(^2Db)6s\ ^3D_1$	9.01e-01	7.97e-01	7.71e-01	D	3.25e-04	9.64e-04	7.92e-04	E	0.0009
12,767.77	0.12	$5d^7(^2F)6s\ ^3F_3$	$5d^7(^2F)6s\ ^3F_4$	6.08e+00	4.99e+00	5.19e+00	C	7.37e-04	7.65e-04	6.28e-04	D+	0.0094
12,900	300	$5d^7(^4P)6s\ ^3P_1$	$5d^7(^4P)6s\ ^3P_0$	1.54e+01	1.46e+01	1.46e+01	D+					0.0094
13,049.56	0.14	$5d^7(^4F)6s\ ^3F_2$	$5d^7(^2G)6s\ ^1G_4$					1.01e-04	5.93e-05	5.19e-05	D	0.0000
452,590	180	$5d^7(^2Db)6s\ ^3D_2$	$5d^7(^4P)6s\ ^3P_1$	2.22e-05	5.68e-05	5.98e-05	E	1.43e-11	1.57e-11	1.32e-11	D	0.0000
1,187,000	6000	$5d^8\ ^3F_2$	$5d^8\ ^3P_0$					6.66e-15		2.89e-14		0.0000
1,607,700	2000	$5d^7(^2P)6s\ ^1P_1$	$5d^7(^4P)6s\ ^3P_2$	9.01e-08				6.30e-14				0.0000
1,797,300	2300	$5d^7(^2P)6s\ ^3P_2$	$5d^7(^2F)6s\ ^3F_3$	3.20e-06				1.32e-15				0.0000

Notes.

[a] The Ritz wavelength and its uncertainty. The wavelengths are in standard air for the λ = (2000–20000) Å region and in vacuum outside this region. Conversion between air and vacuum was made with the five-parameter formula of Peck & Reeder (1972). Wavelength uncertainties are determined in the level optimization procedure (see Section 4).

[b] Level designations and their energies from Table 2. Two columns for energies are dropped from this condensed table.

[c] The scaled A-values (in s^{-1}) for M1 and E2 components from MCDHF, HFR+CPOL, and HFR calculations. The scaling was carried out with the help of transition energies computed from Table 2.

[d] Accuracy codes of the A-values are explained in Table 4.

[e] Absolute branching fraction for the line is calculated from the MCDHF values.

(This table is available in its entirety in machine-readable form.)

calculations using two different versions of GRASP codes with varying sets of configurations for the Os I isoelectronic sequence, including Au IV. For the Au IV spectrum, about 70,000 E1-type transitions were computed with A-values for 551 levels of $5d^8$, $5d^7 6s$, $5d^7 6p$, $5d^6 6s^2$, and $5d^6 6s 6p$ configurations. The GRASP2K calculations were found converging with smaller sets of configurations, and the comparison with experimental energy values was found to be in reasonable agreement for levels of the ground $5d^8$ configuration only. Although among atomic structure codes the GRASP calculations are considered to be more accurate, the accuracy of those calculations is still a subject of debate for heavy elements, such as gold with open d-shells, and large numbers of configurations sets are often required to build the internal consistency of the computed quantities, for example, comparisons of transition probabilities in length and velocity forms.

To check the quality of these calculations, we have made a gross comparison for the energy levels computed with the LSF of Cowan's code calculations, described in Section 6.1, with those computed by Taghadomi et al. (2022). Their data were accessed from the opacity database (Stancil et al. 2021). It has been found that the fractional energy differences vary between 5% and 15%, and the gross disagreement for A-values was found to be accurate within two to three orders of magnitude for lines in the $(5d^8+5d^7 6s)$–$5d^7 6p$ transition array. Though the strong transitions with $S \geqslant 10$ agree within 125%, having better agreement, and there was 500% for $S \in [4, 10)$, the deviations were more than three orders of magnitude for the remaining weak lines. These large deviations even for strong lines could be due to poor computation of the LS composition vectors in the GRASP calculations. Similarly large deviations (200% for $S \geqslant 10$, 500% for $S \in [3, 10)$, and more than three orders of magnitudes for other weak lines) were also noticed for the comparisons of the HULLAC code results for Au IV by Tanaka et al. (2020), therefore we argue that our computed radiative parameters for Au IV are expected to be more accurate than those from previous works (Tanaka et al. 2020; Taghadomi et al. 2022), as we considered an extensive set of almost all interacting configurations in our calculations (see Table 3). This motivated us to provide large-scale data for computing the opacity of Au IV in the kilonova ejecta. Nonetheless, from the HFR calculations described in Section 6.1, only a selected set of configurations, $5d^8$, $5d^7(6s+7s+6d)$, $5d^6 6s^2$, $5d^7(6p+7p+5f)$, and $5d^6 6s 6p$, for which most of the interacting configurations have been accounted for, has been considered for the computation of radiative transition parameters. This resulted in computing the radiative line parameters for about 95,000 E1-type transitions between 1070 levels of the selected configuration sets mentioned above. All those data were supplemented by us (doi:10.5281/zenodo.7788722). It should be noted that the LS composition vectors provided for the levels have little physical meaning due to very high configuration mixing, but they are kept in the supplementary table (of energy levels) for bookkeeping purposes only.

9. Conclusion

A critically evaluated set of data for the Au IV ion has been presented in the wavelength region 500–2106 Å. Theoretical interpretation has been done using Cowan's suite of codes, which works on the formalism of the pseudorelativistic HFR method. 981 spectral lines have been used to optimize 139 energy levels of $5d^8$, $5d^7 6s$, and $5d^7 6p$ configurations. All previously reported levels have been confirmed, except one $J = 2$ level of $5d^7 6p$, which is revised now. Also, three new levels, including the only missing $^1S_0$ level of the ground configuration $5d^8$, have been established. Uncertainties have been provided for all the observed and Ritz wavelengths of the spectral transitions. The intensities of the observed lines have been reduced to a common scale. The line list of Au IV has also been supplemented with Ritz wavelengths of about 830 possibly observable lines and their gA-values. Additionally, Ritz wavelengths and radiative parameters of about 800 forbidden (M1- and E2-type) lines have also been provided. For evaluation of the uncertainty of the transition probability data, comparisons have been made between the calculations of the HFR, HFR+CPOL, and MCDHF methods. The overall agreement was found to be fairly good within the three sets of computations. This enabled us to calculate the radiative lifetimes of the $5d^8$ and $5d^7 6s$ levels. Besides these, large-scale atomic data with specific application to compute the opacity of Au IV in the kilonova ejecta have been supplemented in this work.

Acknowledgments

A.T. would like to duly acknowledge Dr. Y. N. Joshi (late) for giving the spectral plates of gold. The authors are highly thankful to Dr. Alexander Kramida of NIST, Gaithersburg, for providing the updated version of the Cowan (1981) codes (Kramida 2017) and for helpful discussions regarding various computational problems. P.Q. is Research Director of the Belgian National Fund for Scientific Research (F.R.S.-FNRS), from which the financial support is very much appreciated. Some of the atomic calculations in Mons were supported by the Consortium des Equipements de Calcul Intensif (CECI) funded by the F.R.S.-FNRS.

ORCID iDs

Aashna Zainab https://orcid.org/0000-0002-2801-4717
K. Haris https://orcid.org/0000-0002-1341-6297
Sébastien Gamrath https://orcid.org/0000-0002-9115-590X
Pascal Quinet https://orcid.org/0000-0002-3937-2640
A. Tauheed https://orcid.org/0000-0003-3856-5042

References

Abbott, B. P., Abbott, R., Abbott, T. D., et al. 2017, ApJL, 848, L12
Bartos, I., Huard, T. L., & Márka, S. 2016, ApJ, 816, 61
Bromley, S. J., Johnson, C. A., Ennis, D. A., et al. 2020, ApJS, 250, 19
Cowan, R. D. 1981, The Theory of Atomic Structure and Spectra (Berkeley, CA: Univ. California Press)
Fontes, C. J., Fryer, C. L., Hungerford, A. L., Wollaeger, R. T., & Korobkin, O. 2020, MNRAS, 493, 4143
Fraga, S., Karwoswski, J., & Saxena, K. 1976, Handbook of Atomic Data (Amsterdam: Elsevier)
Froese Fischer, C. 2009, PhST, 134, 014019
Froese Fischer, C., Gaigalas, G., Jönsson, P., & Bieroń, J. 2019, CoPhC, 237, 184
Froese Fischer, C., Godefroid, M., Brage, T., Jönsson, P., & Gaigalas, G. 2016, JPhB, 49, 182004
Gillanders, J. H., McCann, M., Sim, S. A., Smartt, S. J., & Ballance, C. P. 2021, MNRAS, 506, 3560
Grant, I. P. 2007, Relativistic Quantum Theory of Atoms and Molecules: Theory and Computation (New York: Springer)
Haris, K., Kramida, A., & Tauheed, A. 2014, PhyS, 89, 115403
Hibbert, A. 1974, JPhB, 7, 1417
Joshi, Y. N., Raassen, A. J. J., & van der Valk, A. A. 1991, JOSAB, 8, 1372
Kajino, T., Aoki, W., Balantekin, A. B., et al. 2019, PrPNP, 107, 109

Kasen, D., Metzger, B., Barnes, J., Quataert, E., & Ramirez-Ruiz, E. 2017, Natur, 551, 80
Kasliwal, M. M., Kasen, D., Lau, R. M., et al. 2022, MNRAS, 510, L7
Kato, D., Murakami, I., Tanaka, M., et al. 2021, Japan–Lithuania Opacity Database for Kilonova (2021), v1.0, http://dpc.nifs.ac.jp/DB/Opacity-Database/
Kildiyarova, R. R., Joshi, Y. N., Lumsden, M. A., & Raassen, A. J. J. 1995, CaJPh, 73, 63
Kramida, A. 2013a, FuST, 63, 313
Kramida, A. 2013b, J. Res. Natl Inst. Stand. Technol., 118, 52
Kramida, A. 2013c, J. Res. Natl. Inst. Stand. Technol., 118, 168
Kramida, A. 2014, Atoms, 2, 86
Kramida, A. 2017, A suite of atomic structure codes originally developed by R. D. Cowan adapted for Windows-based personal computers, v1.1, National Institute of Standards and Technology (doi:10.18434/T4/1502500)
Kramida, A., Ralchenko, Y., Reader, J. & NIST ASD Team 2022a, NIST Atomic Spectra Database, v5.10 (Gaithersburg, MD: National Institute of Standards and Technology), http://physics.nist.gov/asd
Kramida, A., Ryabtsev, A. N., & Young, P. R. 2022b, ApJS, 258, 37
Kramida, A. E. 2011, CoPhC, 182, 419
Leckrone, D. S., Johansson, S., Wahlgren, G. M., & Adelman, S. J. 1993, PhST, 47, 149
McCann, M., Bromley, S., Loch, S. D., & Ballance, C. P. 2022, MNRAS, 509, 4723
Papoulia, A., Ekman, J., Gaigalas, G., et al. 2019, Atoms, 7, 106
Peck, E. R., & Reeder, K. 1972, JOSA, 62, 958
Quinet, P., Palmeri, P., Biémont, É., et al. 2006, A&A, 448, 1207
Raassen, A. J. J., Uylings, P. H. M., Joshi, Y. N., & Wyart, J. F. 1994a, PhyS, 49, 682
Raassen, A. J. J., Uylings, P. H. M., Joshi, Y. N., et al. 1994b, PhyS, 49, 180
Rosberg, M., & Wyart, J. F. 1997, PhyS, 55, 690
Stancil, P. C., Zhao, L., Yang, B., & Osborn, A. 2021, Molecular Opacity Project Database at The University of Georgia, https://www.physast.uga.edu/ugamop/index1.html
Su, M. G., Dong, C. Z., Murphy, N., & O'Sullivan, G. 2009, PhRvA, 79, 042507
Taghadomi, Z. S., Wan, Y., Flowers, A., et al. 2022, Atoms, 10, 94
Tanaka, M., Kato, D., Gaigalas, G., & Kawaguchi, K. 2020, MNRAS, 496, 1369
Tanaka, M., Kato, D., Gaigalas, G., et al. 2018, ApJ, 852, 109
Vieira, N., Ruan, J. J., Haggard, D., et al. 2023, ApJ, 944, 123
Villar, V. A., Cowperthwaite, P. S., Berger, E., et al. 2018, ApJL, 862, L11
Wahlgren, G. M. 2011, 2010 NASA Laboratory Astrophysics Workshop, ed. D. R. Schultz, L11
Wahlgren, G. M., Leckrone, D. S., Johansson, S. G., Rosberg, M., & Brage, T. 1995, ApJ, 444, 438
Wu, M.-R., Barnes, J., Martínez-Pinedo, G., & Metzger, B. D. 2019, PhRvL, 122, 062701
Wyart, J. F., Joshi, Y. N., Raassen, A. J. J., Uylings, P. H. M., & Tchang-Brillet, L. 1994, PhyS, 50, 672
Wyart, J. F., Raassen, A. J. J., Uylings, P. H. M., & Joshi, Y. N. 1993a, PhST, 47, 59
Wyart, J. F., Raassen, A. J. J., van het Hof, G. J., & Joshi, Y. N. 1993b, PhyS, 47, 784
Xu, H. L., Svanberg, S., Quinet, P., Palmeri, P., & Biémont, É. 2007, JQSRT, 104, 52
Zainab, A., & Tauheed, A. 2019, JQSRT, 237, 106614